Frequency-Scaling-Based Spaceborne Squint SAR Sparse Imaging

Yufan Song, Jingjing Zhang, Shuang Jin, Guoxu Li, and Hui Bi, *Member, IEEE*

***Abstract*—In synthetic aperture radar (SAR), due to the characteristics of squint data in spaceborne imaging geometry, a more accurate range cell migration correction operation is necessary. Furthermore, imaging degradation due to ignoring range-variant filtering needed for secondary range compression limits SAR imaging. In addition, owing to enormous computational complexity required for squint SAR data processing, the existing imaging methods, for instance, chirp scaling algorithm and range Doppler algorithm, are no longer sufficient, especially for large-scale scenes. In order to solve above problems, this article presents a novel spaceborne squint SAR sparse imaging method, which could not only eliminate the effects of squint to a certain extent, but also improve the performance of focused SAR image. Compared with the matched-filtering-based squint imaging algorithm, the proposed method can obtain the SAR images with higher quality from fully sampled or downsampled echo data.**

***Index Terms*—Frequency scaling, sparse synthetic aperture radar (SAR) imaging, squint SAR.**

I. Introduction

SYNTHETIC aperture radar (SAR) is an active earth observation system that is installed on various flight platforms and has all-weather and all-day surveillance capabilities [1]. Nowadays, it has been widely used in disaster monitoring, resource exploration, military reconnaissance, etc. [2]. Conventional matched filtering (MF)-based SAR imaging algorithms, e.g., range Doppler algorithm with range cell migration correction (RCMC) in the range Doppler domain [3] and the chirp scaling algorithm (CSA) without interpolation operation [4], could obtain a focused image accurately at low squint angle. However, at higher squint, the presence of squint angle will cause the shift of Doppler center, which requires accurate correction in the imaging process [5]. Simultaneously, the widening of the main lobe and the horizontal increase of sidelobes to the edge of range swath will reduce the image quality of spaceborne SAR under the squint case [6]. In order to solve the problems caused by the increase in the squint angle, several methods were proposed. In 1996, a nonlinear frequency modulation (FM) chirp scaling algorithm (NCSA), an extension of CSA, was proposed by Davidson et al. [7], which provided more accurate secondary range compression (SRC) to accommodate the moderate squint angle. As an accurate and efficient MF-based method to achieve range-variant SRC, NCSA makes high-squint SAR imaging possible. In the following decade years, research based on chirp scaling at high squint angle has been developed. In 2001, Yeo et al. [8] proposed a high-squint subaperture algorithm, which focuses SAR image at high squint angle in the stripmap mode. In 2007, Zhang and Zhai [9] introduced a new method for an accurate estimation of Doppler center based on CSA. Simultaneously, Wang et al. [10] proposed an algorithm based on the quartic phase model, which was applied to describe the range-dependent characteristics of SAR signals. In 2009, a new method was proposed by Zhong et al. [11], which was extended from NCSA for focusing the bistatic SAR data under a wide range swath and a large baseline cases. In 2015, to process the highly squinted missile-borne SAR data, Chen et al. [12] presented a novel fractional CSA. Furthermore, in 2014, Tang et al. [13] introduced an $\omega - K$ algorithm to diving missiles carrying SAR, which can handle missiles with wide swaths and high squint angles. Then, Sun et al. [14] constructed an improved $\omega - K$ algorithm for spatial high-magnification L-band SAR imaging. Meanwhile, Fan et al. [15] presented a modified range Doppler algorithm for handling high-squint SAR, which modifies the migration of ranging units in the ranging frequency domain and avoids interpolation operation. However, the above studies discussed the problem of squint imaging with fully sampled echo; how to achieve high-quality imaging from fully sampled and downsampled squint echo data still requires future research.

Sparse signal processing is a theory developed since the 1990s for processing the large amounts of data. In 2001, Cetin and Karl [16] combined a sparse signal processing technique with SAR imaging for the first time. In 2006, Candes et al. [17], [18] used compressed sensing to process data that realized the reconstruction of targets from incomplete samples, thus breaking the requirements of Shannon–Nyquist sampling theory. In 2010, Patel et al. [19] proposed an imaging model based on an accurate observation matrix to achieve sparse image

Manuscript received 4 July 2022; revised 16 August 2022; accepted 2 September 2022. Date of publication 6 September 2022; date of current version 22 September 2022. This work was supported in part by the National Natural Science Foundation of China under Grant 62271248 and Grant 61901213, in part by the Guangdong Basic and Applied Basic Research Foundation under Grant 2020B1515120060, in part by the Natural Science Foundation of Jiangsu Province under Grant BK20190397, in part by the Aeronautical Science Foundation of China under Grant 201920052001, in part by the Fundamental Research Funds for the Central Universities under Grant NE2020004, in part by the University Joint Innovation Fund Project of CALT under Grant CALT2021-11, and in part by the Science and Technology Innovation Project for Overseas Researchers in Nanjing. *(Corresponding author: Hui Bi.)*

The authors are with the Key Laboratory of Radar Imaging and Microwave Photonics, Ministry of Education, Nanjing University of Aeronautics and Astronautics, Nanjing 211106, China, and also with the College of Electronic and Information Engineering, Nanjing University of Aeronautics and Astronautics, Nanjing 211106, China (e-mail: songyufan@nuaa.edu.cn; jingjingzhang@nuaa.edu.cn; aude@nuaa.edu.cn; c31644916@126.com; bihui@nuaa.edu.cn).

Digital Object Identifier 10.1109/JSTARS.2022.3204539

reconstruction by solving an L_1-norm minimization problem. It can use the sparse prior information of the observed scene to reduce the amount of data through sparse sampling, so as to improve the efficiency of data processing. Nevertheless, sparse SAR imaging methods based on the conventional observation matrix can hardly be used in practical applications because of the huge computation in the matrix construction as well as iterative recovery. In order to solve above problems, an approximated observation-based sparse SAR imaging method was introduced and achieved range and azimuth decoupled by constructing an echo simulation operator [20], [21]. It is found that this method could reduce the computational cost of sparse imaging to the same order as MF and make large-scale sparse data processing possible.

In this article, we proposed a novel frequency-scaling-based spaceborne squint SAR sparse imaging method. The proposed method first incorporates a small nonlinear FM component in the received range signals before regular chirp scaling operation. Then, it constructs an approximated observation-based imaging model via NCSA, and finally, considered scene reconstruction is achieved by solving an L_1-norm regularization problem. Compared with MF-based algorithms, i.e., NCSA, the proposed method could reduce sidelobes and suppress clutter, show better SAR imaging performance, and even allow the large-scale sparse imaging from downsampled squint echo.

The rest of this article is organized as follows. In Section II, a brief introduction of NCSA for squint imaging is provided. In Section III, we introduce the proposed spaceborne squint SAR sparse imaging method from model construction to regularization recovery. Experimental results along with the performance analysis based on simulated and real data are shown in Section IV. Finally, Section V concludes this article.

II. Squint SAR Imaging via NCSA

CSA realizes the scale transformation of the chirp signal by FM operation, but it only considers the distance-related RCMC. Ignoring the distance dependence of SRC, CSA could be effectively performed by just changing the frequency rate of range matching filters. Nevertheless, even at moderate squint angle, this approximation will lead to a significant degradation of the image. Therefore, with the increase in the squint angle, the change of SRC is no longer negligible. While the NCSA adds a small nonlinear FM component before regular chirp scaling operation, which resolves the dependence of SRC on distance. In the following, we will introduce the implementation process of NCSA so as to further apply it to the subsequent sparse SAR imaging model. The transmitted chirp signal with carrier frequency f_c and modulation rate K_r can be expressed as

$$s(\tau) = \text{rect}\left(\frac{\tau}{T_r}\right)\exp\left\{j2\pi f_c\tau - j\pi K_r\tau^2\right\} \tag{1}$$

where T_r is the pulse duration and τ is the time of chirp signal, which is also the range time in the SAR system. After the echo signal received by the radar is quadrature demodulated,

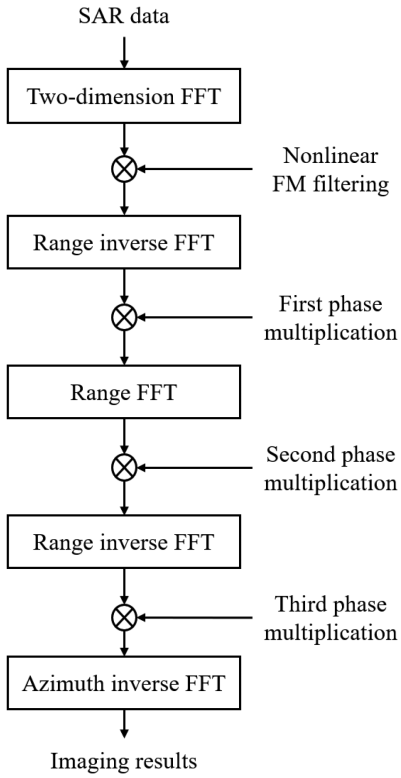

Fig. 1. Flow diagram of NCSA.

the baseband signal of a point target can be written as

$$\begin{aligned} s_r(\eta,\tau;r) = {} & A_0 w_r\left(\tau - \frac{2R(\eta;r)}{c}\right) w_a(\eta-\eta_c) \\ & \cdot\exp\left\{-j\frac{4\pi f_c R(\eta;r)}{c}\right\} \\ & \cdot\exp\left\{-j\pi K_r\left(\tau - \frac{2R(\eta;r)}{c}\right)^2\right\} \end{aligned} \tag{2}$$

where A_0 is the complex constant coefficient, c is the speed of light, η is the azimuth time, $R(\eta;r)$ is the instantaneous range, η_c is the beam center offset time, and w_a and w_r are the azimuth and range weights of the antenna pattern, respectively.

The flow diagram of NCSA is shown in Fig. 1. Before regular CSA processing, the following nonlinear FM filter is added in the 2-D frequency domain, i.e.,

$$\mathbf{H}(f_\eta, f_\tau) = \exp\left\{j\left(\frac{2}{3}\pi A_m f_\tau^3 + \frac{\pi c f_\eta^2 R_r f_\tau^3}{2f_c^4 D(f_\eta,v)^5 v^2}\right)\right\} \tag{3}$$

with a migration factor

$$D(f_\eta, v) = \sqrt{1 - \frac{c^2 f_\eta^2}{4v^2 f_c^2}} \tag{4}$$

where f_η and f_τ are the azimuth range frequencies, respectively, v is the equivalent velocity, R_r is the reference slant range, and A_m is the correction coefficient. The signal trajectory in the

range Doppler domain is

$$\tau_d\left(f_\eta;r\right)=\tau_r\left(f_\eta\right)+\Delta\tau\left(f_\eta;r\right) \tag{5}$$

where $\tau_d(f_\eta;r)$ is the scatterer trajectory of signal, $\tau_r(f_\eta)$ is the reference trajectory, and $\Delta\tau(f_\eta;r)$ is the difference between $\tau_d(f_\eta;r)$ and $\tau_r(f_\eta)$.

After adding the nonlinear FM filter, the signal in the range Doppler domain can be written as (ignoring constant coefficient)

$$\begin{aligned}S_d\left(f_\eta;r\right)=&\,w_r\left[\frac{K_{mr}}{K_r}\left(\tau-\frac{2R\left(\eta;r\right)}{cD\left(f_\eta,v\right)}\right)\right]\\&\cdot W_a\left(f_\eta-f_{\eta c}\right)\exp\left[-j\frac{4\pi R\left(\eta;r\right)}{c}D\left(f_\eta,v\right)f_c\right]\\&\cdot\exp\left[-j\pi K_{mr}\left(\tau-\frac{2R\left(\eta;r\right)}{cD\left(f_\eta,v\right)}\right)^2\right]\\&\cdot\exp\left[-j\frac{2\pi}{3}A_mK_{mr}^3\left(\tau-\frac{2R\left(\eta;r\right)}{cD\left(f_\eta,v\right)}\right)^3\right]\end{aligned} \tag{6}$$

where K_{mr} is the changed range modulation rate at reference slant range. Then, a chirp scaling operation is performed in the range Doppler domain. In order to ensure that all the signals have same range migration after chirp scaling, the desired trajectory $\tau_s(f_\eta;r)$ can be expressed as

$$\tau_s\left(f_\eta;r\right)=\tau_r\left(f_\eta\right)+\Delta\tau\left(f_{\eta r};r\right) \tag{7}$$

where $\Delta\tau(f_{\eta r};r)$ is the difference between $\tau_s(f_\eta;r)$ and $\tau_r(f_\eta)$ at azimuth reference frequency. To obtain the desired trajectory, we need to scale $\Delta\tau(f_\eta;r)$ to $\Delta\tau(f_{\eta r};r)$. Therefore, the chirp scaling operation is completed by multiplying

$$\begin{aligned}\mathbf{H}_1\left(f_\eta,\tau\right)=&\,\exp\left\{-j\pi K_{mr}\left(\alpha-1\right)\left(\tau-\tau_r\right)^2\right\}\\&\cdot\exp\left\{-j\frac{\pi}{3}\left(K_s\left(\alpha-1\right)-2\alpha^2K_{mr}\beta\right)\right.\\&\left.\times\left(\tau-\tau_r\right)^3\right\}\end{aligned} \tag{8}$$

where τ_r is the reference trajectory, α is a scaling factor that is linearly related to $\Delta\tau(f_\eta;r)$ and $\Delta\tau(f_{\eta r};r)$, β represents a nonlinear scale to take into account the nonlinear relationship between $\Delta\tau(f_\eta;r)$ and $\Delta\tau(f_{\eta r};r)$ in an orbital geometry, and K_s is the slope of the variation. After above phase multiplication, the differential range cell migration will be corrected. In order to remove the range dependence of SRC, $\Delta\tau(f_\eta;r)$ needs to be set to zero. Under this constraint, A_m can be expressed as

$$A_m=\frac{K_s\left(\alpha-0.5\right)-\alpha^2K_{mr}\beta}{K_{mr}^3\left(\alpha-1\right)}. \tag{9}$$

Then, after transforming signal to the 2-D frequency domain, the signal is

$$\begin{aligned}S_2\left(f_\eta,f_\tau\right)=&\,W_a\left(f_\eta-f_{\eta c}\right)W_r\left[-\frac{K_s\left(f_\tau+2q\Delta\tau\right)}{K_r\left(K_s+q\right)}\right]\\&\cdot\exp\left\{-j\frac{\pi K_{mr}\left(\alpha-1\right)\Delta\tau^2}{\alpha}\right\}\\&\cdot\exp\left\{-j\frac{4\pi f_cD\left(f_\eta,v\right)R\left(\eta;r\right)}{c}\right\}\\&\cdot\exp\left\{-j\frac{4\pi R_r}{c}\left(\frac{1}{D\left(f_\eta,v\right)}-\frac{1}{D\left(f_{\eta r},v\right)}\right)f_\tau\right\}\\&\cdot\exp\left\{j\left(\frac{\pi f_\tau^2}{\alpha K_{mr}}+\frac{\pi\left(K_s-2\alpha\beta K_{mr}\right)f_\tau^3}{3K_{mr}^3\alpha\left(\alpha-1\right)}\right)\right\}\\&\cdot\exp\left\{-j\frac{\pi}{3}\left[\frac{K_s\left(\alpha-1\right)}{\alpha}-2K_{mr}\beta\left(2-\alpha\right)\right]\right.\\&\left.\times\,\Delta\tau^3\right\}\end{aligned} \tag{10}$$

where $q=K_{mr}(\alpha-1)$, and $\Delta\tau$ is $\Delta\tau(f_\eta;r)$. Range compression and consistent RCMC will be implemented by multiplying

$$\begin{aligned}\mathbf{H}_2\left(f_\eta,f_\tau\right)=&\,\exp\left\{j\frac{4\pi R_r}{c}\left(\frac{1}{D\left(f_\eta,v\right)}-\frac{1}{D\left(f_{\eta r},v\right)}\right)f_\tau\right\}\\&\cdot\exp\left\{-j\left(\frac{\pi f_\tau^2}{\alpha K_{mr}}+\frac{\pi\left(K_s-2\alpha\beta K_{mr}\right)f_\tau^3}{3K_{mr}^3\alpha\left(\alpha-1\right)}\right)\right\}.\end{aligned} \tag{11}$$

It should be noted that the reference azimuth frequency $f_{\eta r}$ has to be out of the azimuth frequency band of the signal. This is due to the fact that the desired trajectory and the scatterer trajectory intersect at $f_{\eta r}$. Therefore, there is no chirp scaling effect on this range line, and hence, the desired effect of eliminating range dependence of SRC could not be obtained.

Finally, azimuth compression and residual phase compensation will be applied in the range Doppler domain by multiplying

$$\begin{aligned}\mathbf{H}_3\left(f_\eta,\tau\right)=&\,\exp\left\{j\frac{4\pi f_cD\left(f_\eta,v\right)R\left(\eta;r\right)}{c}\right\}\\&\cdot\exp\left\{j\frac{\pi K_{mr}\left(\alpha-1\right)\Delta\tau^2}{\alpha}\right\}\\&\cdot\exp\left\{j\frac{\pi}{3}\left[\frac{K_s\left(\alpha-1\right)}{\alpha}-2K_{mr}\beta\left(2-\alpha\right)\right]\right.\\&\left.\times\,\Delta\tau^3\right\}.\end{aligned} \tag{12}$$

Then, the final signal of focused target in the 2-D time domain becomes

$$s_t\left(\eta;r\right)=w_r\left(\tau-\frac{2R\left(\eta;r\right)}{cD\left(f_{\eta r},v\right)}\right)w_a\left(\eta-\eta_c\right)\exp\left[j\theta\left(\eta,\tau\right)\right] \tag{13}$$

where $\theta(\eta,\tau)$ is the phase of the target.

III. High-Squint SAR Sparse Imaging

On the basis of investigating the signal with a high squint angle, we introduce a sparse imaging technique for improving imaging performance. In this section, we first present 1-D sparse imaging model. In the 2-D sparse imaging model, it is still necessary to vectorize echoes and images to be reconstructed during the computation, which leads to huge computational cost. Therefore, we use the approximated observation matrix to construct a high-squint SAR sparse imaging model and reconstruct the sparse image by solving an L_1-norm regularization problem.

A. Observation-Matrix-Based Sparse Imaging

The sparse reconstruction algorithm could be used in 1-D SAR echo data processing. By vectorizing the 2-D backscattering coefficient $\mathbf{X}$ of considered scene and echo data $\mathbf{Y}$, we could obtain the 1-D sparse SAR imaging model

$$\mathbf{y} = \mathbf{\Phi x} \ + \ \mathbf{n_0} \tag{14}$$

where $\mathbf{x} = \mathrm{vec}(\mathbf{X})$, $\mathbf{y} = \mathrm{vec}(\mathbf{Y})$ ($\mathrm{vec}(\cdot)$ represents the superposition of columns), $\mathbf{\Phi}$ is the observation matrix, which is determined by the SAR parameters and imaging geometry relationship, and $\mathbf{n_0}$ is the noise vector. If the considered scene is a sparse scene and, meanwhile, $\mathbf{\Phi}$ satisfies the restricted isometry property condition, $\mathbf{x}$ can be reconstructed by solving

$$\hat{\mathbf{x}} = \min_{\mathbf{X}} \left\{ \|\mathbf{y} - \mathbf{\Phi x}\|_2^2 \ + \ \lambda \|\mathbf{x}\|_1 \right\} \tag{15}$$

where λ is the regularization parameter.

B. Approximated Observation-Based Sparse Imaging

Similar to (14), the 2-D sparse SAR imaging model can be expressed as [22]

$$\mathbf{Y} = \mathbf{\Phi X} + \mathbf{N} \tag{16}$$

where $\mathbf{\Phi}$ is the observation matrix of the considered scene, and $\mathbf{N}$ is the noise matrix. Let $\mathcal{L}(\cdot)$ denote the MF-based SAR imaging operation, such as NCSA in this article. Thus, we have [21], [22]

$$\mathbf{X} = \mathcal{L}(\mathbf{Y}) \tag{17}$$

with

$$\mathcal{L}(\mathbf{Y}) = \mathbf{F}_a^{-1} \left(\left(\left(\left(\mathbf{F}_a \mathbf{Y} \mathbf{F}_r \circ \mathbf{H} \right) \mathbf{F}_r^{-1} \circ \mathbf{H}_1 \right) \mathbf{F}_r \circ \mathbf{H}_2 \right) \mathbf{F}_r^{-1} \circ \mathbf{H}_3 \right) \tag{18}$$

where $\circ$ is the Hadamard product, $\mathbf{F}_a$ and $\mathbf{F}_r$ are the azimuth and range Fourier transforms, respectively, and $\mathbf{F}_a^{-1}$ and $\mathbf{F}_r^{-1}$ are the azimuth and range inverse Fourier transforms, respectively. Let the binary matrices $\mathbf{\Phi}_r$ and $\mathbf{\Phi}_a$ denote the range and azimuth downsampling matrices, respectively. Thus, the 2-D sparse SAR imaging model in (16) can be rewritten as [22]

$$\mathbf{Y} = \mathbf{\Phi}_a \circ \mathcal{G}(\mathbf{X}) \circ \mathbf{\Phi}_r + \mathbf{N} \tag{19}$$

with $\mathcal{G}(\cdot)$ being the procedure of SAR echo data collection (the inverse process of $\mathcal{L}(\cdot)$), i.e.,

$$\mathcal{G}(\mathbf{X}) = \mathbf{F}_a^{-1} \left(\left(\left(\left(\mathbf{F}_a \mathbf{X} \circ \mathbf{H}_3^* \right) \mathbf{F}_r \circ \mathbf{H}_2^* \right) \mathbf{F}_r^{-1} \circ \mathbf{H}_1^* \right) \mathbf{F}_r \circ \mathbf{H} \right) \mathbf{F}_r^{-1} \tag{20}$$

where $(\cdot)^*$ is the conjugate transpose operator.

TABLE I
IST for L_1-Norm-Regularization-Based Sparse SAR Imaging Method via Approximated Observation

Input:	2-D echo data $\mathbf{Y}$;
	Downsampling matrix $\mathbf{\Phi}_\mathrm{a}$
	Downsampling matrix $\mathbf{\Phi}_\mathrm{r}$
Initial:	Iterative parameter μ
	Error parameter ε
	Maximum iterative step $\mathrm{T}_{\max}$
	Scene image $\mathbf{X}^{(0)}$
While	$t \leqslant \mathrm{T}_{\max}$ and Resi $> \varepsilon$
Step 1:	$\mathbf{W}^{(t-1)} = \mathbf{Y} - \mathbf{\Phi}_a \circ \mathcal{M}\left(\mathbf{X}^{(t-1)}\right) \circ \mathbf{\Phi}_r$
Step 2:	$\Delta\mathbf{X}^{(t-1)} = \mathcal{R}\left(\mathbf{\Phi}_a^{\mathrm{T}} \circ \mathbf{W}^{(t-1)} \circ \mathbf{\Phi}_r^{\mathrm{T}}\right)$
Step 3:	$\mathbf{Z}^{(t-1)} = \mathbf{X}^{(t-1)} + \mu\Delta\mathbf{X}^{(t-1)}$
Step 4:	$\lambda^{(t-1)} = \left\|\mathbf{Z}^{(t-1)}\right\|_{K+1} / \mu$
Step 5:	$\mathbf{X}^{(t)} = F_{\lambda\mu,1}\left(\mathbf{Z}^{(t-1)}\right)$
Step 6:	Resi $= \left\|\mathbf{X}^{(t)} - \mathbf{X}^{(t-1)}\right\|_F$
	$t = t+1$
end	
Output:	Recovered sparse image $\hat{\mathbf{X}} = \mathbf{X}^{(i)}$

C. Iterative Recovery

For the model in (16), the scene can be reconstructed by

$$\hat{\mathbf{X}} = \min_{\mathbf{X}} \left\{ \|\mathbf{Y} - \mathbf{\Phi}_a \circ \mathcal{G}(\mathbf{X}) \circ \mathbf{\Phi}_r\|_F^2 + \lambda \|\mathbf{X}\|_1 \right\} \tag{21}$$

where $\hat{\mathbf{X}}$ is the reconstructed 2-D backscattering coefficient. Several algorithms, such as complex approximated message passing and iterative soft thresholding (IST), are available for solving the optimization problem in (21). Without loss of generality, the IST algorithm is selected for the iterative recovery in this article, whose flow diagram is depicted in Fig. 2 [21] and the detailed procedure is listed in Table I, where K represents the sparsity of observed scene. $|\mathbf{Z}^{(t)}|_{K+1}$ is the $(K+1)$th largest element of $|\mathbf{Z}^{(t)}|$. $F_{\lambda\mu,q}(\mathbf{Z}^{(t)})$ is the thresholding operator for matrix $\mathbf{Z}^{(t)}$, i.e.,

$$F_{\lambda\mu,q}\left(\mathbf{Z}^{(t)}\right) = f_{\lambda\mu,1}\left(\mathbf{Z}^{(t)}(n_a, n_r)\right) \tag{22}$$

where $n_a = 1, 2, \ldots, N_a$ and $n_r = 1, 2, \ldots, N_r$. For any $z \in \mathbb{C}$, the thresholding function $f_{\lambda\mu,1}(\cdot)$ is

$$f_{\lambda\mu,1}(z) = \begin{cases} \mathrm{sign}(z)\left(|z| - \lambda\mu\right), & \text{if } |z| \geqslant \lambda\mu \\ 0, & \text{otherwise} \end{cases} \tag{23}$$

where μ controls the speed of algorithm convergence.

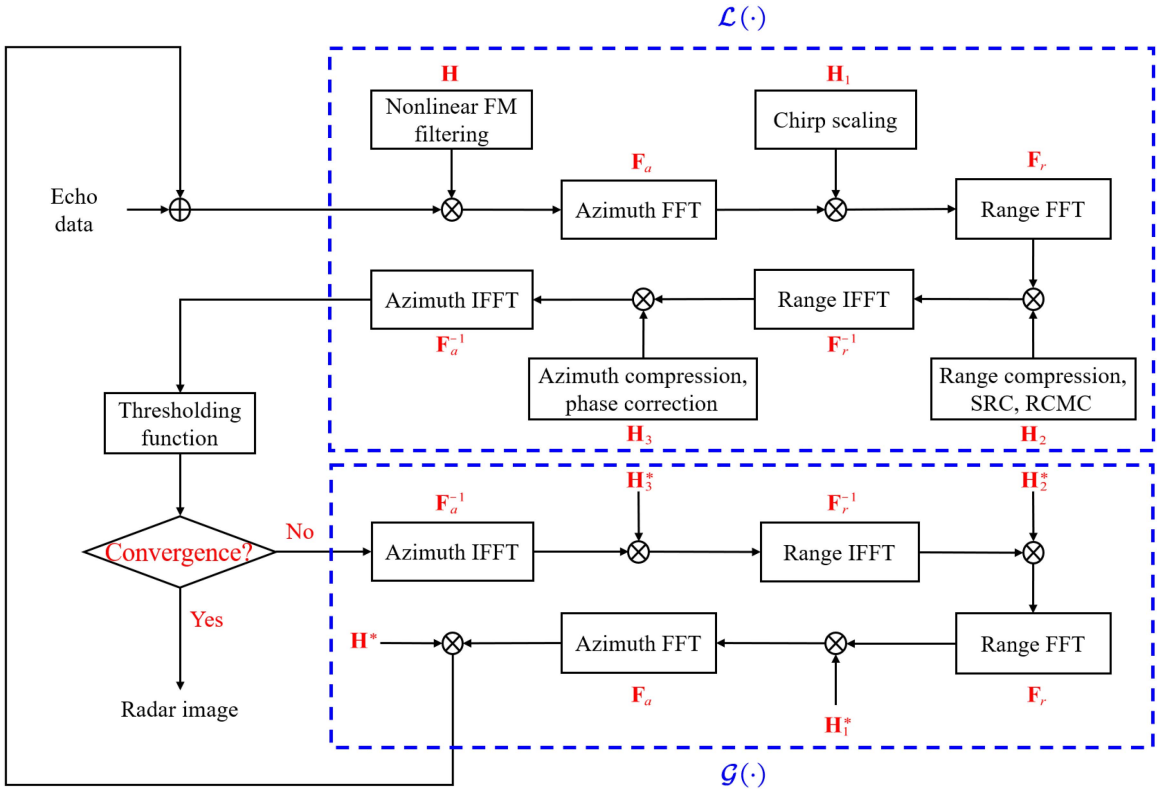

Fig. 2. Flow diagram of the proposed sparse SAR imaging method.

D. Computational Cost Analysis

Assume that the size of 2-D echo data $\mathbf{Y}$ is $N_\eta(\text{Azimuth}) \times N_\tau(\text{Range})$ and the size of discrete surveillance scene $\mathbf{X}$ is $N_P(\text{Azimuth}) \times N_Q(\text{Range})$. Let $M = N_\eta \times N_\tau$ and $N = N_P \times N_Q$; then, the computational complexity of the CSA and NCSA imaging methods can be expressed as $\mathcal{O}(M\log(M))$ [21]. The computation of the proposed method includes two main parts, i.e., the calculations of an inverse and an MF procedure, whose complexity is $\mathcal{O}(M\log(M))$, and a thresholding operation with the complexity $\mathcal{O}(N)$ for each iteration. Let I denote the number of required iterative steps for the accurate reconstruction of the proposed method; thus, its total computational complexity is in the order of $\mathcal{O}(I(M\log(M)+N))$ [21]. Since the proposed algorithm usually converges within ten steps, it means that it has similar computational complexity to traditional MF, which makes the sparse reconstruction of the large-scale scene possible.

IV. Experiments and Performance Analysis

In this section, several experiments based on echo data of point targets and real scenes are used to validate the proposed method. Without loss of generality, we set targets in three different positions (see in Fig. 3), and the squint angle θ is set as 5° and 10°, respectively. T2 is at the scene center; T3 and T1 are 5 km away from T2 in the range and azimuth directions, respectively. The rest of the experimental parameters are listed in Table II. Since the imaging results of three point targets are similar, we only list the recovered image of them from fully sampled echo data with $\theta = 10^\circ$. The rest of the cases only take the imaging results corresponding to T2 as an example.

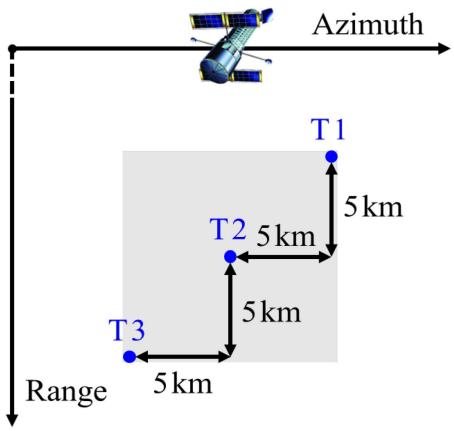

Fig. 3. Target distribution in the simulation.

Fig. 4 shows the imaging results of point targets from fully sampled data by traditional CSA, NCSA, and the proposed sparse imaging method with $\theta = 5^\circ$ and $\theta = 10^\circ$, respectively. It can be seen that due to the existence of squint angle, CSA can no longer recover the point target with significant energy dispersion. However, both the NCSA and the proposed method can obtain a well-focused image of the target even at the scene edges. In the simulation based on full-sampled echo with $\theta = 10^\circ$, we use the peak-to-sidelobe ratio (PSLR) and the integrated sidelobe ratio (ISLR) to compare the sidelobe suppression ability of different

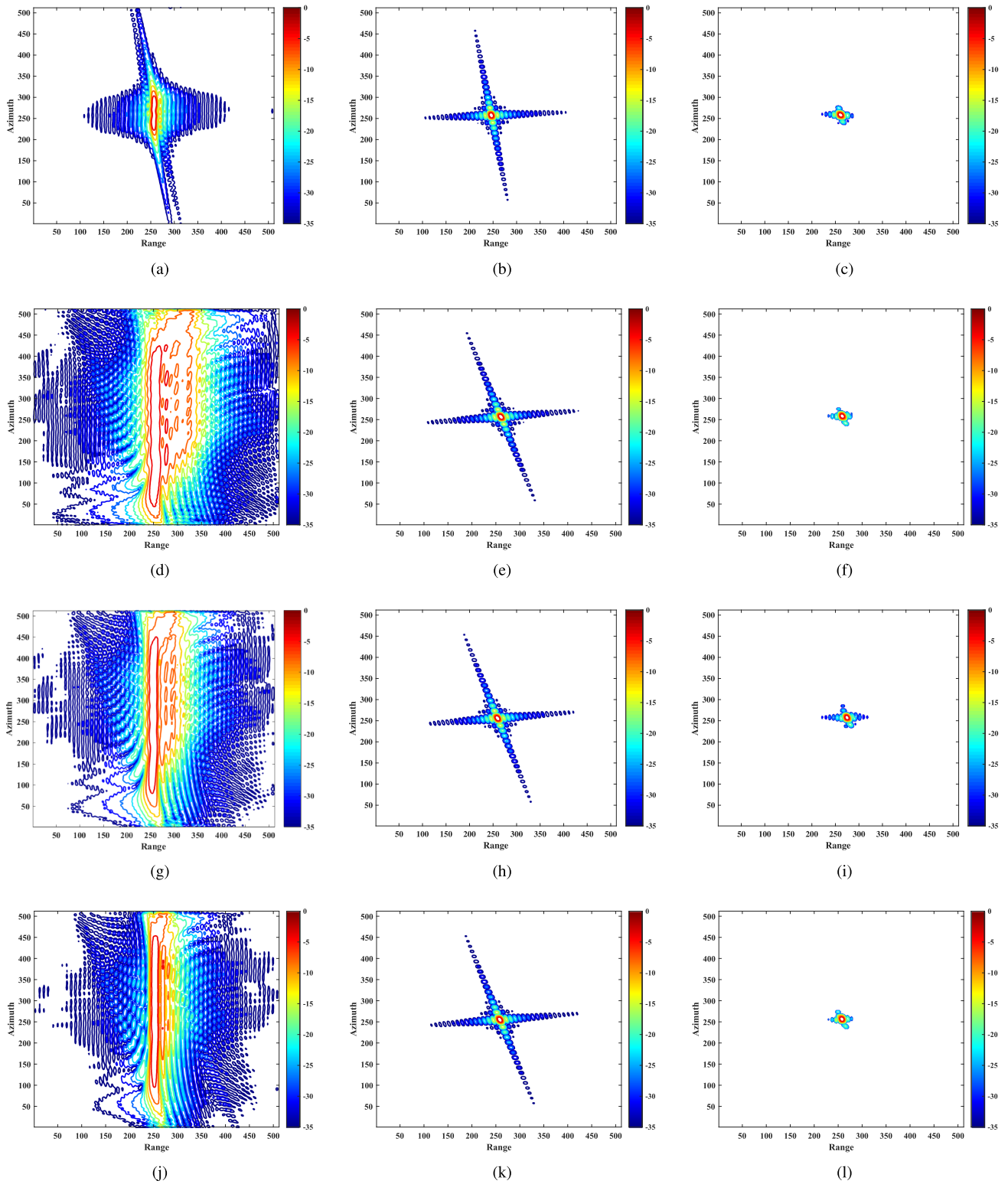

Fig. 4. Reconstructed images of point targets from full-sampled echo data by different methods. (a) T2 + CSA with $\theta = 5°$. (b) T2 + NCSA with $\theta = 5°$. (c) T2 + the proposed sparse imaging method with $\theta = 5°$. (d) T1 + CSA with $\theta = 10°$. (e) T1 + NCSA with $\theta = 10°$. (f) T1 + the proposed sparse imaging method with $\theta = 10°$. (g) T2 + CSA with $\theta = 10°$. (h) T2 + NCSA with $\theta = 10°$. (i) T2 + the proposed sparse imaging method with $\theta = 10°$. (j) T3 + CSA with $\theta = 10°$. (k) T3 + NCSA with $\theta = 10°$. (l) T3 + The proposed sparse imaging method with $\theta = 10°$.

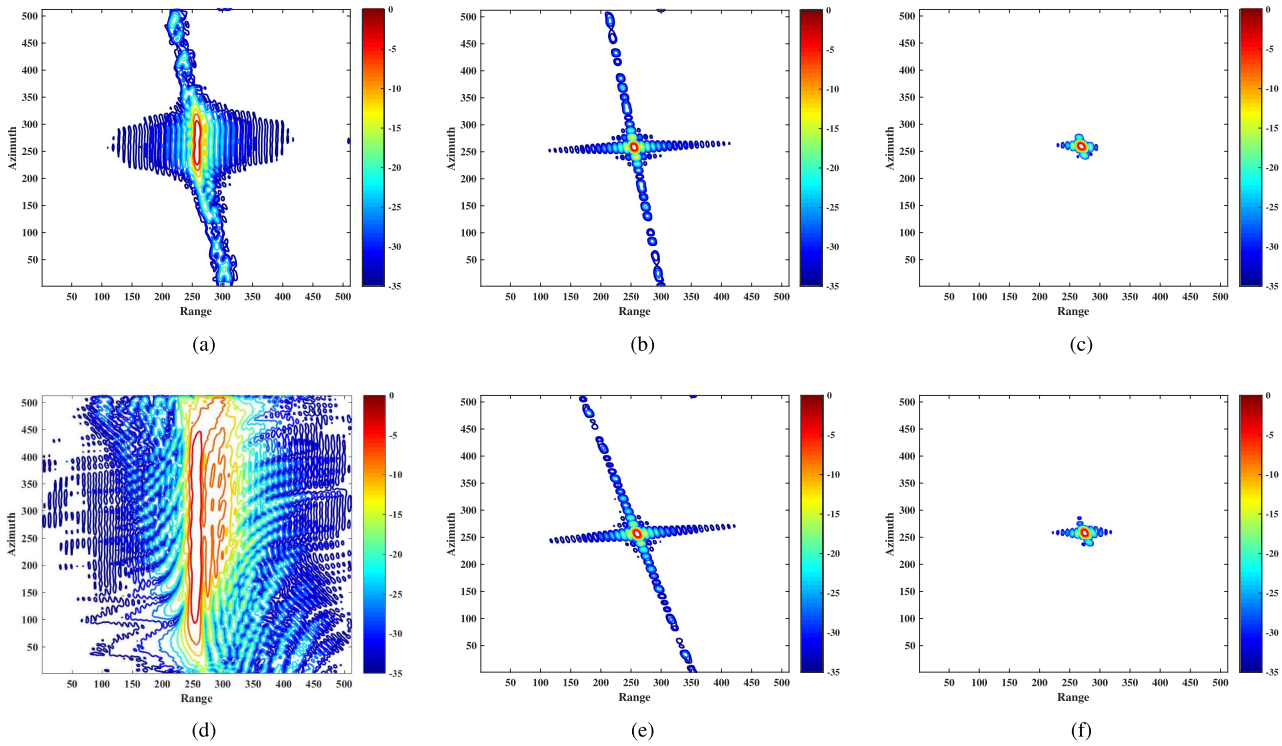

Fig. 5. Reconstructed images of point targets from 25% random downsampling data by different methods. (a) T2 + CSA with $\theta = 5^\circ$. (b) T2 + NCSA with $\theta = 5^\circ$. (c) T2 + the proposed sparse imaging method with $\theta = 5^\circ$. (d) T2 + CSA with $\theta = 10^\circ$. (e) T2 + NCSA with $\theta = 10^\circ$. (f) T2 + the proposed sparse imaging method with $\theta = 10^\circ$.

TABLE II
SIMULATED PARAMETERS

Parameter	Value
Central incidence angle	23.16°
Wavelength	0.03125 m
Azimuth antenna length	3.75 m
Bandwidth	180 MHz
Squint angle	5°, 10°
Pulse width	35 μs
Range sampling rate	203.5 MHz
Orbit semimajor axis	6888100 m
Satellite velocity	7613.7 m/s
Pulse repetition frequency (PRF)	5262 Hz

TABLE III
PLSR OF THE RECONSTRUCTED IMAGE BY DIFFERENT METHODS [DB]

Target	NCSA		Proposed Method	
	PSLRa	PSLRr	PSLRa	PSLRr
T1	−13.25	−13.01	−35.22	−31.98
T2	−13.22	−13.08	−30.23	−36.01
T3	−13.30	−13.18	−34.75	−32.11

TABLE IV
ILSR OF THE RECONSTRUCTED IMAGE BY DIFFERENT METHODS [DB]

Target	NCSA		Proposed Method	
	ISLRa	ISLRr	ISLRa	ISLRr
T1	−10.38	−10.01	−44.48	−41.36
T2	−10.47	−10.34	−39.24	−39.42
T3	−10.49	−10.06	−41.27	−44.83

methods. The results are shown in Tables III and IV, respectively. Since the results of the CSA have been severely defocused, we only calculate the PLSR and the ISLR of the NCSA and the proposed method for comparison. It shows that compared to NCSA-based results, the images reconstructed by the proposed method show better quality with less sidelobes. To further support our viewpoint, we perform 25% random sampling for the collected fully sampled echo of a point target with $\theta = 5^\circ$ and $\theta = 10^\circ$. Fig. 5 shows the imaging results of different methods. From Fig. 5, it is found that due to the lack of data and existence of high squint, the CSA has been unable to recover the target. The other MF-based algorithm, i.e., NCSA, could also not recover the target anymore with severe energy dispersion in the azimuth direction. However, the proposed method reconstructs the point target with better performance even under the high-squint case.

In order to quantitatively evaluate the noise and clutter suppression capability of the proposed method, we introduce the

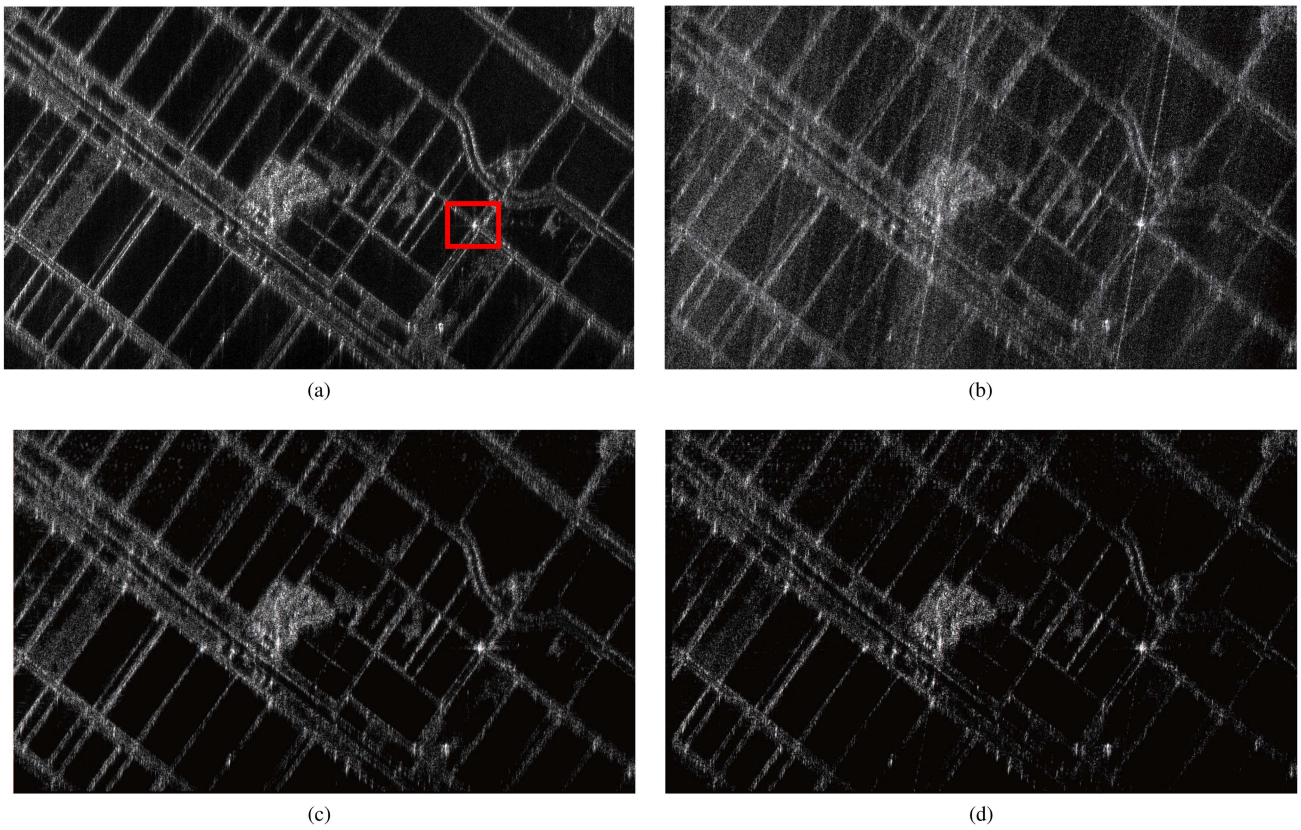

Fig. 6. Reconstructed image of salt pan area by different methods. (a) NCSA with 100% samples. (b) NCSA with 25% samples. (c) Proposed sparse imaging method with 100% samples. (d) Proposed sparse imaging method with 25% samples. $\theta = 5^\circ$.

TABLE V
TBR OF THE RECONSTRUCTED IMAGE BY DIFFERENT METHODS [DB]

T2	$\theta = 5^\circ$		$\theta = 10^\circ$	
	100%	25%	100%	25%
CSA	31.36	28.79	15.28	15.83
NCSA	45.91	42.93	45.59	43.89
Proposed method	72.55	89.55	68.55	66.33

TABLE VI
TBR OF THE RECONSTRUCTED IMAGE BY DIFFERENT METHODS [DB] (MARKED BY THE RED BOX)

Target	Fig. 6		Fig. 7	
	100%	25%	100%	25%
NCSA	33.55	31.24	39.48	34.02
Proposed method	38.27	41.68	43.37	43.78

target-to-background ratio (TBR) to validate the performance of different methods [23], which is defined as

$$\text{TBR} \triangleq 20\log_{10}\left(\frac{\max_{(p,q)\in\mathcal{I}}\left|(\mathbf{X})_{(p,q)}\right|}{(1/N_{\mathcal{B}})\sum_{(p,q)\in\mathcal{B}}\left|(\mathbf{X})_{(p,q)}\right|}\right) \tag{24}$$

where $\mathcal{I}$ represents the target area, $\mathcal{B}$ represents the background region near $\mathcal{I}$, and $N_{\mathcal{B}}$ is the number of pixels in $\mathcal{B}$. Table V shows the TBR values of the images recovered by different methods with $\theta = 5^\circ$ and $\theta = 10^\circ$, respectively. It can be seen that whether using fully sampled or downsampled data, TBR values in the recovered images of the proposed method averaged over 65 dB, significantly outperforming CSA and NCSA.

Furthermore, we introduce the proposed method to process the echo of real large-scale scenes. The sizes of the scenes in Figs. 6 and 7 are both 921 (azimuth) $\times$ 1600 (range) and the computation times of Figs. 6(c), (d), 7(c), and (d) are 9.66, 146.79, 10.95, and 141.51 s, respectively. Similarly, we calculate the TBR values of the target regions as an example (marked by the red box) in Figs. 6 and 7, and the results are shown in Table VI. Fig. 6 shows the reconstructed image of the sparse salt pan area by different methods with $\theta = 5^\circ$. Fig. 7 depicts the imaging results of the coastal scene by different methods at $\theta = 10^\circ$. From Figs. 6 and 7, it is clearly seen that the reconstructed images by the NCSA with 25% samples have obvious azimuth energy dispersion, thus causing failed recovery. However, similar to above simulated results, the proposed method could also achieve the high-squint sparse imaging of complicated scenes even from 25% downsampled data. In addition, it also has better image performance with less noise and clutter.

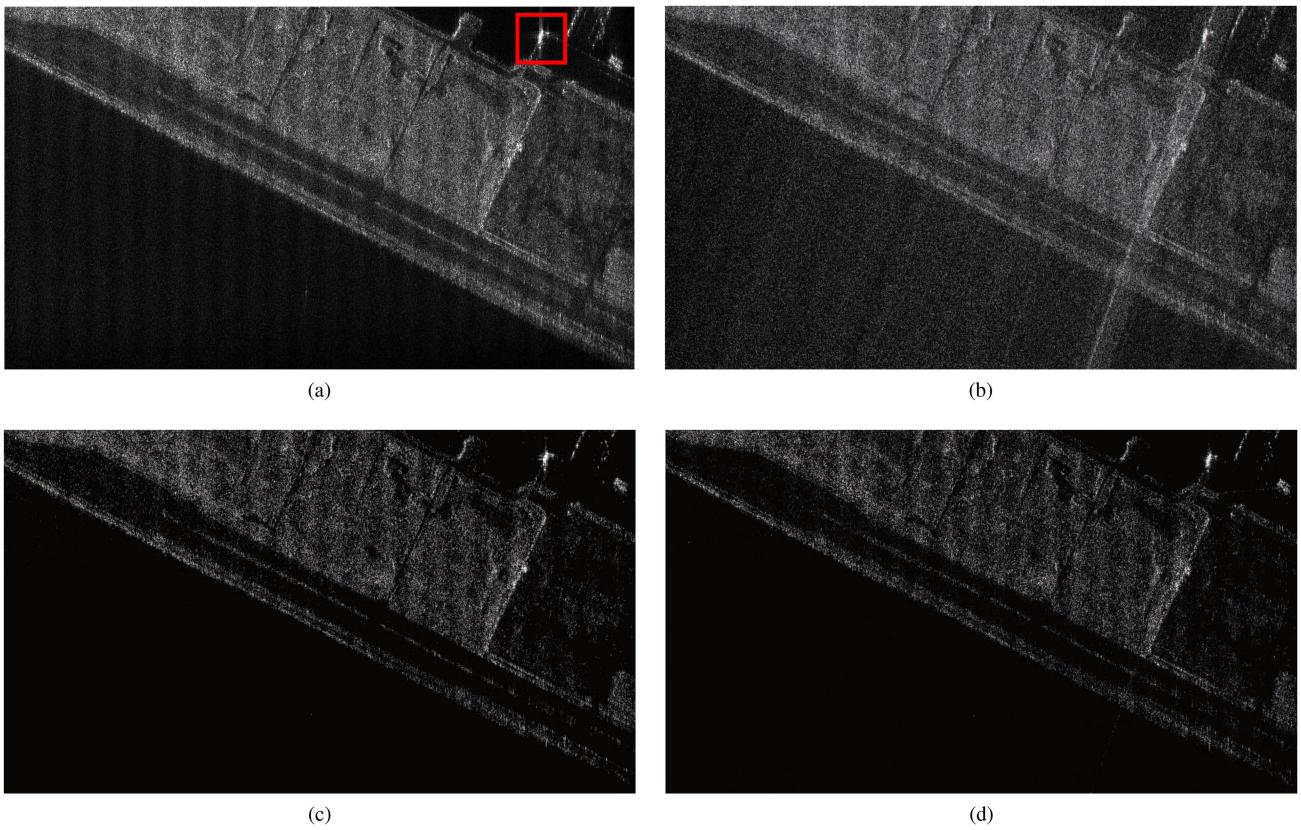

Fig. 7. Reconstructed image of the coastal scene by different methods. (a) NCSA with 100% samples. (b) NCSA with 25% samples. (c) Proposed sparse imaging method with 100% samples. (d) Proposed sparse imaging method with 25% samples. $\theta = 10^{\circ}$.

V. Conclusion

In this article, a novel spaceborne squint SAR sparse imaging method was proposed and applied to real data processing. With the help of approximated observation, the proposed method made the sparse reconstruction of large-scale scenes possible. Furthermore, experimental results showed that the proposed method can eliminate the degradation of image quality caused by the squint angle and effectively reduce the sidelobes, noise, and clutter compared with MF-based algorithms. In addition, it also shows the high-quality imaging ability of the sparse surveillance area from downsampled data.

References

[1] J. C. Curlander and R. N. Mcdonough, *Synthetic Aperture Radar: System and Signal Processing*. New York, NY, USA: Wiley, 1991.
[2] I. G. Cumming and F. H. Wong, *Digital Processing of Synthetic Aperture Radar Data: Algorithms and Implementation*. Norwood, MA, USA: Artech House, 2004.
[3] I. G. Cumming and J. Bennett, "Digital processing of seasat SAR data," in *Proc. IEEE Acoust., Speech, Signal Process.*, Washington, DC, USA, 1979, pp. 710–718.
[4] H. Runge and R. Bamler, "A novel high precision SAR focussing algorithm based on chirp scaling," in *Proc. IEEE Int. Geosci. Remote Sens. Symp.*, Houston, TX, USA, 1992, pp. 372–375.
[5] R. K. Raney, H. Runge, R. Bamler, I. G. Cumming, and F. H. Wong, "Precision SAR processing using chirp scaling," *IEEE Trans. Geosci. Remote Sens.*, vol. 32, no. 4, pp. 786–799, Jul. 1994.
[6] G. W. Davidson and I. G. Cumming, "Signal properties of spaceborne squint-mode SAR," *IEEE Trans. Geosci. Remote Sens.*, vol. 35, no. 3, pp. 611–617, May 1997.
[7] G. W. Davidson, I. G. Cumming, and M. R. Ito, "A chirp scaling approach for processing squint mode SAR data," *IEEE Trans. Aerosp. Electron Syst.*, vol. 32, no. 1, pp. 121–133, Jan. 1996.
[8] T. S. Yeo, N. L. Tan, C. Zhang, and Y. Lu, "A new subaperture approach to high squint SAR processing," *IEEE Trans. Geosci. Remote Sens.*, vol. 39, no. 5, pp. 954–968, May 2001.
[9] Y. Zhang and W. Zhai, "A new method for Doppler centroid estimation for spaceborne SAR based on chirp scaling algorithm," in *Proc. IEEE Int. Geosci. Remote Sens. Symp.*, 2007, pp. 543–546.
[10] K. Wang and X. Liu, "Quartic-phase algorithm for highly squinted SAR data processing," *IEEE Geosci. Remote Sens. Lett.*, vol. 4, no. 2, pp. 246–250, Apr. 2007.
[11] H. Zhong and X. Liu, "An extended nonlinear chirp-scaling algorithm for focusing large-baseline azimuth-invariant bistatic SAR data," *IEEE Geosci. Remote Sens. Lett.*, vol. 6, no. 3, pp. 548–552, Jul. 2009.
[12] S. Chen, S. Zhang, H. Zhao, and Y. Chen, "A new chirp scaling algorithm for highly squinted missile-borne SAR based on FrFT," *IEEE J. Sel. Topics Appl. Earth Observ. Remote Sens.*, vol. 8, no. 8, pp. 3977–3987, Aug. 2015.
[13] S. Tang, L. Zhang, P. Guo, and Y. Zhao, "An Omega-K algorithm for highly squinted missile-borne SAR with constant acceleration," *IEEE Geosci. Remote Sens. Lett.*, vol. 11, no. 9, pp. 1569–1573, Sep. 2014.
[14] L. Sun, Z. Yu, C. Li, W. Liu, S. Wang, and J. Geng, "An imaging algorithm for spaceborne high-squint L-band SAR based on time-domain rotation," *IEEE J. Sel. Topics Appl. Earth Observ. Remote Sens.*, vol. 12, no. 12, pp. 5289–5299, Dec. 2019.
[15] W. Fan, M. Zhang, J. Li, and P. Wei, "Modified range-Doppler algorithm for high squint SAR echo processing," *IEEE Geosci. Remote Sens. Lett.*, vol. 16, no. 3, pp. 422–426, Mar. 2019.
[16] M. Cetin and W. C. Karl, "Feature-enhanced synthetic aperture radar image formation based on nonquadratic regularization," *IEEE Trans. Image Process.*, vol. 10, no. 4, pp. 623–631, Apr. 2001.
[17] E. J. Candes, J. Romberg, and T. Tao, "Robust uncertainty principles: Exact signal reconstruction from highly incomplete frequency information," *IEEE Trans. Inf. Theory.*, vol. 52, no. 2, pp. 489–509, Feb. 2006.

[18] H. Nyquist, "Certain topics in telegraph transmission theory," *Trans. Amer. Inst. Elect. Eng.*, vol. 47, no. 2, pp. 617–644, Apr. 1928.
[19] V. M. Patel, G. R. Easley, D. M. Healy Jr., and R. Chellappa, "Compressed synthetic aperture radar," *IEEE J. Sel. Topics Signal Process.*, vol. 4, no. 2, pp. 244–254, Apr. 2010.
[20] J. Fang, Z. Xu, B. Zhang, W. Hong, and Y. Wu, "Fast compressed sensing SAR imaging based on approximated observation," *IEEE J. Sel. Topics Appl. Earth Observ. Remote Sens.*, vol. 7, no. 1, pp. 352–363, Jan. 2014.
[21] H. Bi, G. Bi, B. Zhang, W. Hong, and Y. Wu, "From theory to application: Real-time sparse SAR imaging," *IEEE Trans. Geosci. Remote Sens.*, vol. 58, no. 4, pp. 2928–2936, Apr. 2020.
[22] H. Bi, B. Zhang, X. X. Zhu, W. Hong, and Y. Wu, "L_1 regularization based SAR imaging and CFAR detection via complex approximated message passing," *IEEE Trans. Geosci. Remote Sens.*, vol. 55, no. 6, pp. 3426–3440, Jun. 2017.
[23] M. Cetin, W. C. Karl, and D. A. Castanon, "Feature enhancement and ATR performance using nonquadratic optimization-based SAR imaging," *IEEE Trans. Aerosp. Electron. Syst.*, vol. 39, no. 4, pp. 1375–1395, Oct. 2003.

Yufan Song was born in Hebei, China, in 1999. She received the bachelor's degree in electronics and information engineering from the University of Electronic Science and Technology of China, Chengdu, China, in 2020. She is currently working toward the Ph.D. degree in information and communication engineering with the Nanjing University of Aeronautics and Astronautics, Nanjing, China.

Her current research interests include sparse microwave imaging, synthetic aperture radar data processing, and their applications.

Jingjing Zhang was born in Anhui, China, in 1986. He received the B.E. degree in electronic information engineering from the University of Science and Technology of China, Hefei, China, in 2009, and the Doctor of Engineering degree in signal and information processing from the University of Chinese Academy of Sciences, Beijing, China, in 2017.

From 2017 to 2021, he was with the School of Information Science and Technology, Fudan University, Shanghai, China. Since 2021, he has been an Associate Professor with the College of Electronics and Information Engineering, Nanjing University of Aeronautics and Astronautics, Nanjing, China. His research interests include the design, modeling, and calibration of polarimetric synthetic aperture radar (SAR) systems, SAR imaging, and polarimetric and polarimetric interferometric SAR signal processing and applications.

Shuang Jin was born in Liaoning, China, in 1998. She received the bachelor's degree in electronics and information engineering from Dalian Jiaotong University, Dalian, China, in 2020. She is currently working toward the master's degree in electronics and information engineering with the Nanjing University of Aeronautics and Astronautics, Nanjing, China.

Her main research interests include synthetic aperture radar (SAR) tomography and differential SAR tomography.

Guoxu Li was born in Shandong, China, in 1998. He received the bachelor's degree in electronics and information engineering from the Shandong Jiaotong University, Jinan, China, in 2021. He is currently working toward the master's degree in electronic information with the Nanjing University of Aeronautics and Astronautics, Nanjing, China.

His current research interests include sparse synthetic aperture radar (SAR) mode design and SAR imaging.

Hui Bi (Member, IEEE) was born in Shandong, China, in 1991. He received the bachelor's degree in electronics and information engineering from Yantai University, Yantai, China, in 2012, and the Ph.D. degree in signal and information processing from the University of Chinese Academy of Sciences, Beijing, China, in 2017.

From 2012 to 2017, he was with the Science and Technology on Microwave Imaging Laboratory, Institute of Electronics, Chinese Academy of Sciences, Beijing. From 2017 to 2018, he was a Research Fellow with the School of Electrical and Electronic Engineering, Nanyang Technological University, Singapore. Since 2018, he has been with the College of Electronic and Information Engineering, Nanjing University of Aeronautics and Astronautics, where he is currently a Professor. His main research interests include sparse microwave imaging with compressive sensing, synthetic aperture radar data processing and application, sparse signal processing, and 3-D/4-D synthetic aperture radar imaging.